Title

Si photocathode with Ag-supported dendritic Cu catalyst for CO2 reduction

Journal

Energy and Environmental Science, 12(3)

ISSN

1754-5692

Authors

Gurudayal
Beeman, JW
Bullock, J
et al.

Publication Date

2019-03-01

DOI

10.1039/c8ee03547d

Peer reviewed

Si Photocathode with Ag-Supported Dendritic Cu Catalyst for CO_2 Reduction†

Gurudayal,[a,b] Jeffrey W. Beeman,[a,c] James Bullock,[d] Hao Wang,[e,f] Johanna Eichhorn,[a] Clarissa Towle,[b,c] Ali Javey,[c,d] Francesca M. Toma,[a] Nripan Mathews,[e,f] and Joel W. Ager*[,a,b,c]

Si photocathodes integrated with Ag-supported dendritic Cu catalysts are used to perform light-driven reduction of CO_2 to C_2 and C_3 products in aqueous solution. A back illumination geometry with an n-type Si absorber was used to permit the use of absorbing metallic catalysts. Selective carrier collection was accomplished by a p^+ implantation on the illumination side and an n^+ implantation followed by atomic layer deposition of TiO_2 on the electrolyte site. The Ag-supported dendritic Cu CO_2 reduction catalyst was formed by evaporation of Ag followed by high-rate electrodeposition of Cu to form a high surface area structure. Under simulated 1-sun illumination in 0.1 M $CsHCO_3$ saturated with CO_2, the photovoltage generated by the Si (~600 mV) enables C_2 and C_3 products to be produced at -0.4 vs RHE. Texturing of both sides of the Si increases the light-limited current density, due to reduced reflection on the illumination side, and also deceases the onset potential. Under simulated diurnal illumination conditions photocathodes maintain over 60% faradaic efficiency to hydrocarbon and oxygenate products (mainly ethylene, ethanol, propanol) for several days. After 10 days of testing, contamination from the counter electrode is observed, which causes an increase in hydrogen production. This effect is mitigated by a regeneration procedure which restores the original catalyst selectivity. A tandem, self-powered CO_2 reduction device was formed by coupling a Si photocathode with two series-connected semitransparent $CH_3NH_3PbI_3$ perovskite solar cells, achieving an efficiency for the conversion of sunlight to hydrocarbons and oxygenates of 1.5% (3.5% for all products).

Broader Context

Sunlight-driven conversion of carbon dioxide and water into useful chemical and fuels is of fundamental and technological interest. Widespread adoption of such a technology could slow the rate of carbon dioxide emissions into the atmosphere by replacing chemicals obtained from oil with sustainably generated alternatives. Here, a silicon-based photocathode is coupled to inexpensive halide perovskite solar cells, producing C_{2+} products with an efficiency greater than that of photosynthesis.

Introduction

An environmentally sustainable future will require significant changes in all aspects of energy conversion.[1,2] Developing an alternative to unsustainable fossil fuel extraction and combustion is a critical priority to slow down and eventually stabilize the rise of CO_2 levels in the atmosphere and in the oceans.[3] A number of technical approaches have been proposed to use renewable energy sources to convert CO_2 to useful chemicals and/or fuels, including thermochemical, high temperature electrochemical, thermolysis electrochemical and photoelectrochemical (PEC) methods.[4] Of these, systems which replicate the functions of photosynthesis,[5,6] which synthetically converts CO_2 to more reduced forms (Photosystem I and Calvin cycle) and oxidize water to oxygen (Photosystem II), are both intellectually and technologically interesting.[7–9]

There is an analogy between the Z-scheme configuration of photosystems I and II and a tandem solar cell, as both generate chemical potential differences in their sub-components that add together to produce electricity or drive a chemical reaction. In the case of photosynthesis, the generated chemical potential difference enables the requisite carbon dioxide reduction and oxygen evolution reactions (CO_2R and OER, respectively) to occur.[10] Indeed, this concept has been utilized in solar-driven electrochemical water splitting devices which produce hydrogen as the reduction product.[11,12] A commonly-used motif in these types of devices is the use of high and low band gap absorbers to maximize the attainable voltage.[13] Either or both of the absorbers can be in contact with the electrolyte, forming a photocathode in the case of the reduction reaction and a photoanode in the case of oxidation.[11,14,15]

Solar-driven electrochemical CO_2R has the potential to efficiently and selectively drive the production of energy dense hydrocarbons and provide an alternative to fossil fuels that can exploit existing infrastructures, thus becoming more appealing than the similar approach used for hydrogen production. Also, it is notable that for systems driven by CO_2 dissolved in an aqueous electrolyte, the mass transfer limited current density, which on the order of a few 10's of mA cm^{-2},[16] are a good match to the current densities provided by solar cells under 1 sun illumination.[17] For this reason, photocathodes which drive CO2R reactions directly would be expected to perform well in this light limited photocurrent regime.

Although far fewer in number compared to water splitting, there have been a number of recent demonstrations of solar-powered CO_2R, some of which have reported overall energy conversion efficiencies above 1%.[18–26] Notably, most of these demonstrations employ photovoltaic elements which are isolated from the electrochemistry; exceptions are studies which use an illuminated photoanode to drive the water

oxidation reaction (OER) with a dark cathode employed for CO_2R.[20,21] Urbain et al. reported a CO_2 reduction prototype reactor containing a Si photoanode coupled to Ni foam as an OER catalyst and a Cu foam with Zn flakes as the cathode with a solar to syngas conversion efficiency of 4.3%.[25] Significantly, Asadi et al. combined a 3 junction amorphous Si solar cell with a WSe_2 CO_2R catalyst to make an artificial leaf, achieving an overall 4.6% conversion efficiency to all products and a 20% FE for CO.[27] In the solar thermal study of Marxer et al., a 4 kW solar reactor was coupled to a porous ceria catalyst to achieve a solar to CO conversion efficiency of 5.25%.[26]

Thus, a photocathode which can drive the CO_2 reduction reaction is desirable for increasing the design space of CO_2R devices in general and also enabling the fabrication of integrated devices.[11] However, there relatively few reports of photoelectrochemical reduction of CO_2 using semiconducting photoelectrodes.[28–31] Halman reported in 1978 the formation of formic acid, formaldehyde, and methanol by p-GaP photoanodes,[32] although later work by Sears and Morrison associated some of the observed products with corrosion processes.[33] There are intriguing reports of methanol formation from III-V photocathodes,[34–36] but the mechanism by which this product forms has not been clarified.[37–40] Also notable are studies which interface molecular catalysts to p-Si to produce 2-electron reduction products such as CO.[41,42] An example of this type of study is the work of Song and co-workers in which a Si photocathode with a nanoporous Au thin film produced CO with 96% faradaic efficiency (FE).[43] Graphene has also been used as a co-catalyst for selective conversion of CO_2 to CO using p-Si nanowire photocathodes.[44]

Natural photosynthesis produces C_3 and C_4 sugars.[45] The question thus arises whether a light-driven artificial system can make C-C coupled products with equivalent or, ideally, greater efficiency. From the point of view of economic value and commercial market size, C_{2+} hydrocarbons and oxygenates are desirable due to their high energy densities and compatibility with the established petroleum processing infrastructure.[4,46] In electrocatalytic investigations of CO_2 reduction, heterogeneous catalysts, specifically Cu and bimettalic alloys containing Cu, are employed to produce C-C coupled products as they can generate C_2 and even C_3 products.[47–51] While there are exceptions, when heterogeneous CO_2 reduction catalysts are coupled to photocathodes, a product distribution similar to that of the electrocatalyst operated by itself is produced, albeit with a cathodically shifted onset potential due to the photovoltage.[52] However, there are only a few reports of the formation of C-C coupled products using CO_2R photocathodes. As one example, Nakato and co-workers employed p-Si interfaced with Cu nanoparticles to produce a C_2 (ethylene) and C_1 (CO, methane) products although a full faradaic efficiency analysis was not performed.[53]

The challenge of performing photocathodic conversion of CO_2 to C_2 and C_3 products (e.g. ethylene, ethanol, propanol) forms the motivation for this study. The architecture we employed is shown schematically in Fig. 1. In contrast to prior Si photocathode studies we chose n-type silicon as the absorber, using charge selective contacts to control the device polarity.[54–56] Selective hole collection was achieved by a p^+ implanted layer on the illumination face, along with texturing to reduce the reflectivity and maximize the number of absorbed photons.

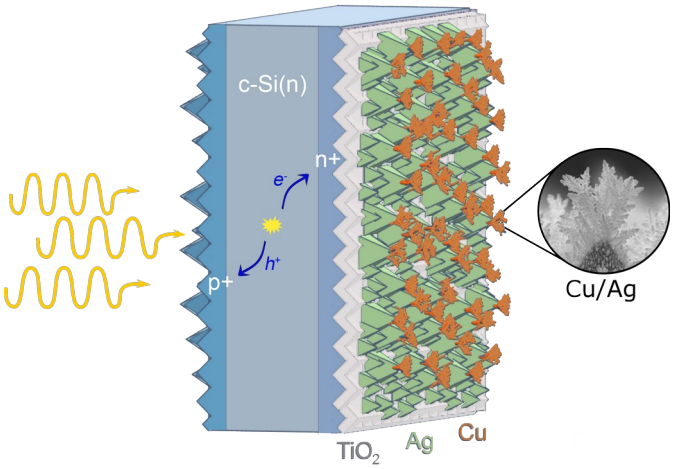

Fig. 1. Schematic of textured Si photocathode. The illuminated face has a p^+ layer for selective collection of holes from the n-Si absorber. TiO_2 is used to selectively collect electrons and passivate the textured surface. An Ag-supported dendritic Cu catalyst is used to drive CO_2 reduction to C_2/C_3 products.

The choice of materials on the side of the photocathode which will contact the electrolyte requires significant care. An n^+ implanted layer was used to create a selective electron contact, and a textured surface was employed to increase the surface area available for catalysis. A thin (10 nm) layer of TiO_2 was used to perform 3 functions: (1) passivate the surface, (2) transport electrons to the catalyst, and (3) prevent in-diffusion of Cu from the catalyst into the Si. Finally, we employed an electrochemically deposited high surface area Ag-supported dendritic Cu catalyst which we have previously shown to produce C_2 products (hydrocarbons and oxygenates) over a wide range of voltage and current density operating conditions.[23] A number of studies have shown that high surface area, dendritic catalysts, can support relatively high current densities for CO_2R.[57–60] For example, Urbain et al reported that Ag dendrites formed on Cu foam have high activity (>27 mA cm^{-2}) and selectivity (85-96%) for CO formation.[57]

Here, we will show that an integrated photocathode can achieve overall CO_2R with faradaic efficiencies (FEs) of over 80%, with faradaic efficiencies (FEs) to C_2–C_3 products as high as 70%. Notably, we developed a method to regenerate the catalytic surface and demonstrated continuous operation over 20 diurnal illumination cycles. The back illuminated geometry is well suited for integration with a higher band gap absorber situated optically and electrically in series. Using this design, we demonstrated integrated, unbiased CO_2 reduction using two semi-transparent halide perovskite solar cells coupled to the photocathode, achieving a 1-sun overall solar to chemical energy conversion efficiency of 3.5% (1.5% to hydrocarbons and oxygenates).

Results and Discussion

Si photocathode for CO_2 reduction

Figure 2 shows the electrocatalytic interface comprised of the textured Si and Ag-supported dendritic Cu CO_2R catalyst (see ESI for fabrication details). It can be seen that the electrochemical deposition method we employed favours nucleation at the tips of the texture pyramids, Fig. 2a, creating a "nano-cactus" morphology formed by Cu dendrites ~100 nm in length (also see Figs. S7a-c, ESI). Figure 2b shows that the catalyst completely covers the textured Si. We found that complete coverage of the pyramids was essential to sustain the CO_2 reduction process. In cases of less complete coverage, hydrogen production became dominant over time, which would be expected if exposed TiO_2 were reduced to Ti metal, which is known to be a catalyst for the hydrogen evolution reaction (HER).[47] Au-supported dendritic Cu catalysts were also fabricated by a similar process; they also have a high-branched morphology, Figs. S7d-e, S8 in ESI. XRD and XPS analyses were used to show that Cu partially covers the support metal and that both metals are exposed at the surface (Figs. S9 and S10).

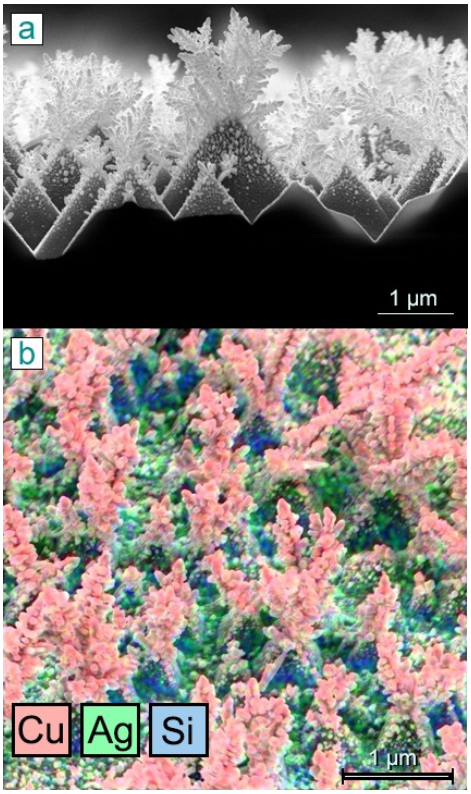

Fig. 2. Structure of Si photocathode with Ag-supported dendritic Cu catalyst. **a,** Cross-sectional SEM image of textured Si photocathode integrated catalyst. **b,** EDX elemental mapping in plan view.

Photoelectrochemical (PEC) measurements were carried out in 0.1 M $CsHCO_3$ electrolyte (pH = 6.8), under simulated sunlight illumination at AM 1.5G 100 mW cm^{-2} from a 150 W Xenon lamp (see ESI for details). We and others have previously shown that use of the Cs^+ cation, as opposed to the more typically used K^+, encourages formation of C_{2+} products on Cu-based catalysts.[59,61,62] A three-electrode electrochemical configuration was used (Fig. 3a and Fig. S2), using a Si photocathode as the working electrode, an Ag/AgCl reference electrode, and an IrO_2 counter electrode; both electrodes had an active area of 1 cm^2. An anion conduction membrane was used to separate the cathode and anode chambers of the cell.

Figure 3b compares the linear sweep voltammograms for textured and planar photocathodes with the Ag-supported dendritic Cu catalyst. Data from a dark planar cathode (n^+ wafer with the same catalyst but without the hole-selective p^+ back contact, see ESI Fig. S1 for implantation profiles) are also shown. Neither photocathode generates cathodic current in the dark, as expected from the presence of the hole-selective back contact which blocks electrons in the absence of light. The dark control displays a current onset at about -0.75 V vs. RHE, which is similar to what we have observed previously for these types of Ag-supported dendritic Cu catalysts by themselves.[23] For both photocathodes, there is a cathodic shift of the onset potential due to the photovoltage from the Si, and the expected light-limited current density is observed at larger cathodic potentials. The textured photocathode has both a less cathodic onset potential and a higher current density at all potentials compared to the planar control, which we attribute to superior light capture on the illumination side and to effective selective charge collection and suppression of surface recombination at both interfaces. From the shift of the J-V curve of the planar photocathode compared to the dark control, a photovoltage of 550-650 mV is inferred (see ESI for calculation details and Fig. S14). These values are comparable to those achieved with implanted contacts in other PEC applications.[63,64] Similar JV data for photocathodes with AuCu catalysts are shown in Fig. S12, ESI.

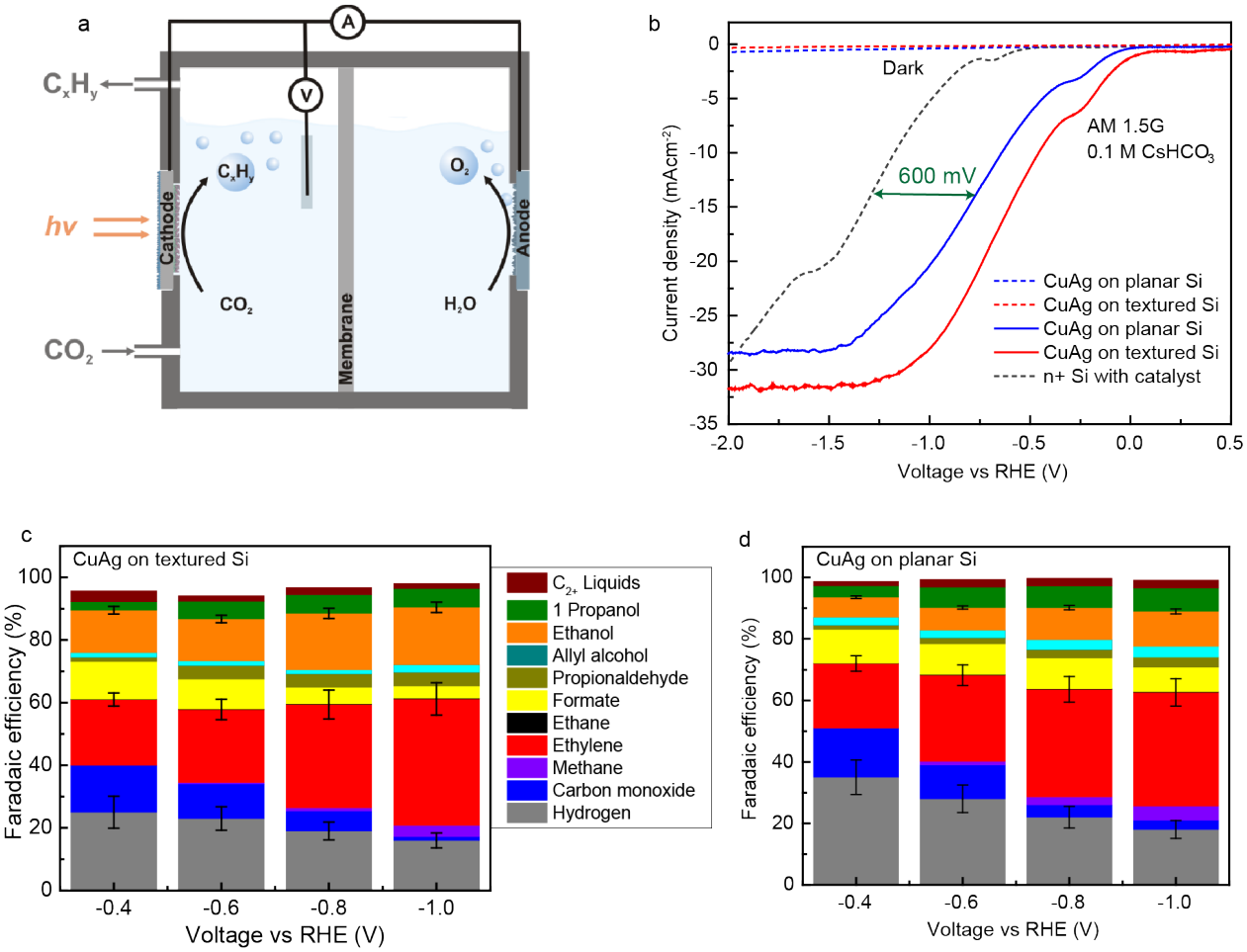

Fig. 3. a. Schematic of the membrane-separated PEC cell. b. Photocurrent-potential curve of Si photocathodes in three electrode configuration and under dark and simulated 1 Sun (AM 1.5G, 100 mW cm^{-2}) illumination. The grey dotted line shows data from the dark cathode (Ag-supported dendritic Cu on n+/ n-Si), while the solid grey double sided arrow shows the generated photovoltage (~600 mV) for the planar photocathode. c. Faradaic efficiency of textured Si photocathode with Ag-supported dendritic Cu. d. Faradaic efficiency of CuAg deposited planar Si photocathode with Ag-supported dendritic Cu. C_{2+} liquids in Fig. 3c and Fig. 3d refer to acetate, acetaldehyde, glyoxal, glycolaldehyde, ethylene glycol and hydroxyacetone. The electrolyte in all cases was in 0.1 M $CsHCO_3$, pH 6.8. Error bars show the standard deviation from repeated experiments. See ESI Figs. S5 and S6 for examples of raw data used to generate the FE plots.

Figures 3c and 3d show the product distribution for the illuminated planar and textured photocathodes with the Ag-supported dendritic Cu catalyst at voltages between -0.4 and -1.0 V vs. RHE. At a given voltage the product distribution for photocathodes is similar and both show a trend of decreasing H_2 production (i.e. increasing selectivity to CO_2 reduction) as the potential increases. Similar CO_2R product distributions were observed when testing the Si photocathode with an Au-supported dendritic Cu catalyst (Fig. S13, ESI). Interestingly, even though the geometric current density for the textured photocathode is very high (~30 mA cm^{-2}) at the maximum power point, -1.0 V vs. RHE, we did not observe evidence of CO_2 depletion due to mass transfer limitations at the catalyst surface, which would have resulted in an increased rate of H_2 production. We attribute the ability to operate at high current densities, on the order of the light limited current density for a Si absorber, to the high surface area of the integrated catalyst (electrochemically active surface area of the Ag-supported dendritic catalysts is about an order of magnitude larger than evaporated Cu deposited on planar Si, see Fig. S11 and ESI for details). Electrochemical impedance spectroscopy (EIS) analyses were also carried out to evaluate the charge transfer behaviour from planar and textured photocathodes (See ESI and Figs. S3 and S4).

At all potentials in Fig. 3c and 3d, CO_2R is the dominant reaction, with the FE for the competing hydrogen evolution reaction (HER) decreasing with increasing cathodic bias; at -1.0 V vs. RHE the FE for HER is very low: only 16% and 18% for the planar and textured photocathodes, respectively. Within the CO_2R products, ethylene is dominant at all potentials, and ethanol has the highest FE among the oxygenates, followed by 1-propanol. The planar and textured Si photocathodes show similar selectivity (79% ± 6% and 78% ± 5%) for hydrocarbons and oxygenates at -1.0 V vs RHE. These values are substantially higher than those achieved by previously reported Si photocathodes at under similar conditions,[65] which we attribute to the large loading of the catalyst and the back illumination geometry.

To determine whether there are any major differences in the product distribution under dark and light driven conditions, we selected potentials, which produce similar current densities, and thus similar local CO_2 concentration and pH, for

the two cases. For a current of 10 mA cm^{-2}, examination of Fig. 3b shows that a bias of -1.1 V vs RHE is required for the dark cathode and -0.55 V vs RHE for the planar Si photocathode respectively. Evaluation of the product distribution under these conditions did not reveal any significant differences, as we expected for our design (Fig. S15, ESI). To evaluate the specific role of Ag support, we fabricated Cu-supported dendritic Cu catalysts of similar morphology on planar n^+-Si; these had comparatively lower selectivity to C-C coupled products and to CO2R in general (see ESI and Figs. S28 and S29 for details.)

Evaluation and Management of Stability

Solar to chemical energy conversion schemes must operate stably for years to be environmentally and economically viable.[66–68] This is particularly important for integrated devices, as failure of any one of the components would require remanufacturing of the entire device. We simulated diurnal cycling by operating textured photocathodes at -0.4 V vs RHE and under 1-sun conditions for 10 hours followed by 14 hours off. After each day of testing, the electrolyte was replaced and an analysis of the liquid products was performed (gas products were measured every 15 minutes during illuminated operation). The pH of the electrolyte was measured to evaluate the dissolved CO_2 concentration, which remained close to the expected saturation value (see ESI for details and Fig. S27). Figures 4a and b show the results of 10 days of testing of a Si photocathode. The current density was relatively constant in the range of ~8-10 mA cm^{-2}, with a small increase in the first 8 days, followed by a decrease (Fig. S16). However, after 2 days, the FE for H_2 production, initially only 20%, began to increase, reaching nearly 60% after 10 days. The FEs for the major CO_2R products — ethylene, ethanol, and propanol — decreased, particularly near the end of the test period, while the FE for CO was found to rise. We note that under these test conditions, the measured total FE for all products can be less than 100%, which is attributed to the evaporation of some liquid products over the 10-hour test period due to the continuous purging of the cell with CO_2.

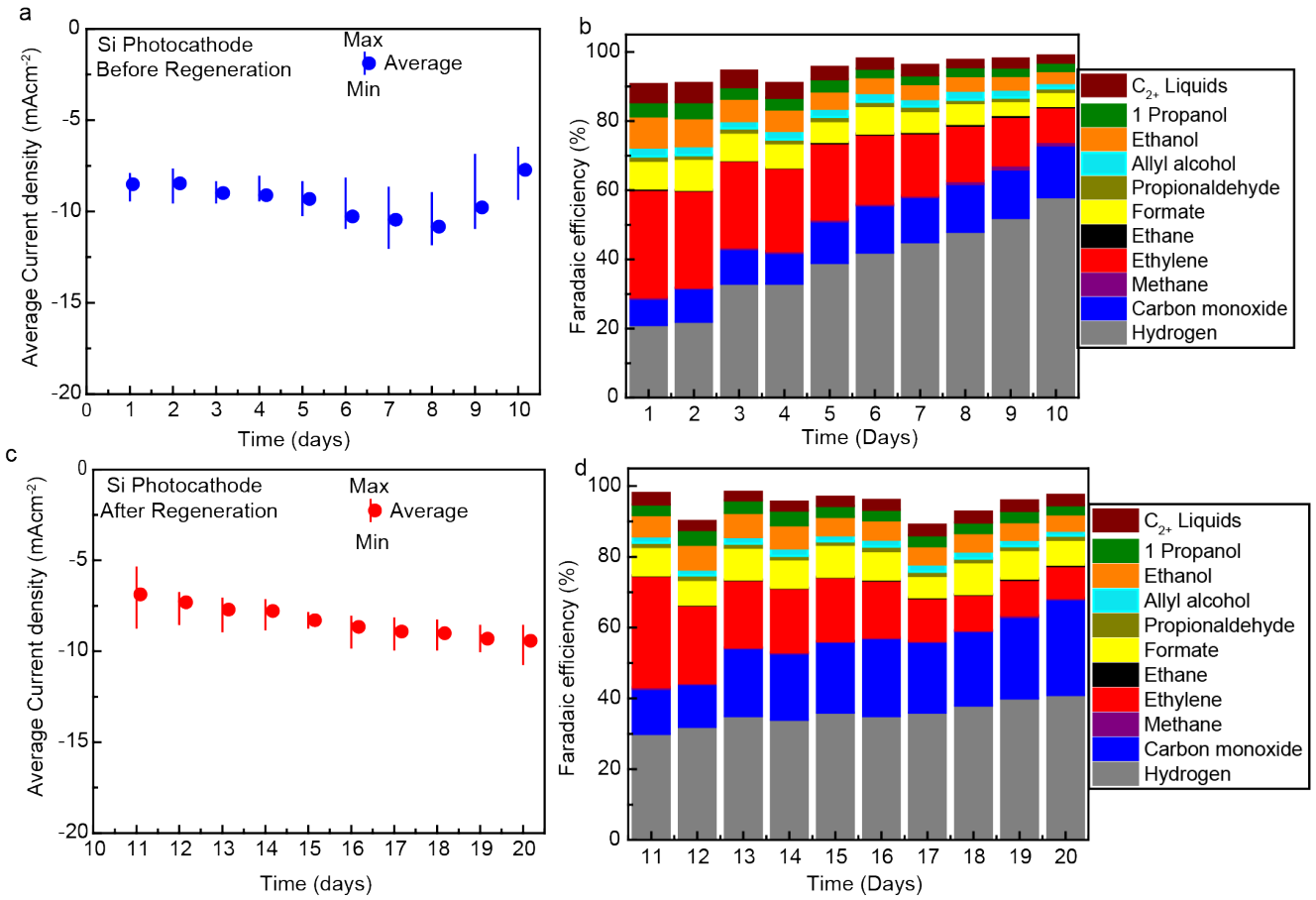

Fig. 4. Stability measurement of a textured silicon photocathode with an integrated Ag-supported dendritic Ag catalyst at -0.4 V vs RHE in 0.1 M $CsHCO_3$ electrolyte solution under simulated 1-sun illumination. Simulated diurnal cycling was performed with 10 hrs light on and 14 hrs light off. The electrolyte was changed after each daily measurement of the liquid products. a. Daily average photocurrent over 10 days of the Si photocathode before regeneration of the catalyst. Current density data points were averaged over a day; the vertical line indicates the maximum and minimum current density on that day. b. CO_2R product distribution with time. c. Daily average/high/low photocurrent of the Si photocathode after Cu catalyst regeneration. d. CO_2R product distribution with time of the regenerated photocathode.

The origin of the decrease in the CO_2R selectivity during sustained operation was investigated. Examination of the catalyst after 10 days of operation by SEM revealed no apparent changes in its morphology (Fig. S17, ESI). However, XPS analysis of the photocathode surface revealed the presence of Ir (Fig. S18c, ESI), to which we attribute the increasing H_2 selectivity. This type of cathode contamination by metals from the counter electrode has been observed

previously in CO_2 electrolysis cells and appears to be only partially mitigated by the use of an anion conducting membrane.[24] Replacing the IrO_2 counter electrode with Pt exacerbated the contamination effect with H_2 production becoming dominant after only 2 days (Fig. S19c, ESI, shows XPS observation of Pt on the photocathode). Use of CoPi as a counter electrode increased the required cell voltage by 1 V, but appeared to mitigate somewhat cathode contamination (Figs. S25 and S26, ESI). This material could be an alternative, less costly, anode if the overpotential could be reduced to values comparable to IrO_2.

To mitigate contamination from the counter electrode, we developed a catalyst regeneration scheme, which consists of careful mechanical removal of some of the copper from the photocathode surface and redeposition of fresh dendritic Cu using our electrochemical process (See ESI for photocathode regeneration process and Fig. S20). A similar regeneration strategy was used previously to extend the lifetime of a Si photoanode used for water oxidation.[64] Figures 4c and d summarize the results of an additional 10 days of testing of a regenerated photocathode. Comparing the FEs for Day 10 and Day 11 (Figs. 4b and 4d), it is clear that the regeneration process restores the selectivity for CO_2 reduction, with the selectivity of the competing hydrogen evolution reaction being reduced from 60% to 30%.

Compared to Day 1, the current density immediately after regeneration (Day 11) was slightly lower, and the FEs for H_2 (30% v 22%) and CO (12% v8%) were higher. Examination of the morphology of the regenerated catalyst finds the Cu redeposition tends to nucleation and grow on existing dendrites as opposed to on the underlying Ag (Fig. S21, ESI), leading to more Ag sites exposed to the electrolyte, which is consistent with the increased FE to CO. Notably, the regenerated photocathode maintains selectivity to CO_2R longer than the originally fabricated one. Both the current density and the FE for H_2 increase with time, both of which could be attributed to cross-contamination from the counter electrode, but the rate of increase of the FE for H_2 production is slower, reaching only 40% on Day 20. The slower loss of selectivity can be attributed to the higher loading of Cu on the regenerated catalyst, so that contaminants occupy a smaller fraction of the overall surface area.

Self-powered CO_2 reduction device

A self-powered CO_2R device must provide the thermodynamic potential for the desired reduction reaction at the cathode and for water oxidation at the anode, plus overpotentials and voltage losses in the cell. The thermodynamic potential for CO_2R is 1.1-1.3 V depending on the product, the overpotential for C_{2+} product formation is ca. 1.0 V, the overpotential for water oxidation is ca. 0.4 V at the current densities we employ,[23] and the cell losses are estimated at 0.2 V. Adding these values leads to target voltage of 2.7 V. As the Si photocathode can provide up to 0.6 V, additional driving elements must provide at least 2.1 V. This analysis leads to our choice of two semi-transparent halide perovskite solar cells, as this class of cells has both a tunable band gap in the range of 1.6-2.0 eV and a relatively high open circuit voltage compared to other materials with similar band gaps (Fig. S23). To couple the perovskite solar cells optically in series with the Si photocathode, they must be semi-transparent, transmitting light below their band gaps to the Si. Historically, it has been difficult to make semi-transparent halide perovskite solar cells with similar performance to opaque cells due to cell damage occurring during the fabrication of the transparent contact. Here, we used a very low energy sputtering process to form this contact, which resulted in cells of acceptable performance for this application (see ESI for cell fabrication details).

To form a self-powered CO_2 reduction device, two semi-transparent halide perovskite ($CH_3NH_3PBI_3$) solar cells were connected electrically in series with the PEC cell, using a geometry similar to one employed previously for water splitting.[69,70] The cells have a band gap of 1.58 eV and 1-sun performance parameters as follows: short circuit current (J_{SC}) = 14.5 mA cm^{-2}, open circuit voltage (V_{OC}) = 1.06 V, fill factor (FF) = 0.55, and an overall power conversion efficiency (PCE) =8.4%. Figure 5a depicts the device geometry with two semi-transparent cells masked to expose 0.5 cm^2 used as top absorbers and a Si photocathode with an active area of 1 cm^2 was used as the bottom absorber (see also photo, Fig. S22, ESI).

As shown in Fig. 5b, the two series-connected semitransparent solar cells (0.5 cm^2 each) provide a V_{oc} of 2.1 V and a short circuit current (I_{sc}) of 5.8 mA under 1-sun (AM 1.5G, 100 mW cm^{-2}) illumination, with the voltage meeting the minimum criterion discussed above. A range of electrolyte concentration (0.1 – 0.5 M $CsHCO_3$) was used to investigate the role of resistance losses in the electrochemical cell. Two-electrode measurements of the Si photocathode itself and shaded by the perovskite solar cells are also shown in Figs. S24 and 5b. At a given voltage, the current in the photoelectrochemical cell increases with increasing electrolyte concentration, as would be expected due to the increased ion conductivity The operating current (I_{op}) of the tandem device (perovskite/Si photocathode) is determined by the crossing point of the absolute photocurrent of Si photocathode and series-connected perovskite solar cells, Fig. 5b. The operating currents were 2.1 to 2.9 mA at 1.95 to 1.86 V and in 0.1 to 0.5 M $CsHCO_3$ electrolyte concentrations, respectively.

The solar to chemical conversion performance of the tandem system was monitored by measuring the evolution of CO_2R products without external bias under constant 1-sun illumination for 1.75 hr (Fig. 5c). The FE for H_2 was relatively unaffected by the electrolyte concentration while the FE for ethylene increased and the FE for the C_1 products CO and formate decreased. The solar-to-chemical conversion (STC) efficiency was calculated by the equation:

$$\eta_{STCi} = \sum \frac{I_{op} \times E_i^o \times FE_i}{P_{in}} \quad (1)$$

where, I_{op} is operating current, E^o_i is the thermodynamic potential of the respective product, FE_i is the Faradaic efficiency of the individual product and P_{in} is input power. There are more than 12 products generated and thus the total solar to chemical conversion (η_{STC}) efficiency is sum of all these individual conversion efficiencies (η_{STCi}). The STC conversion

efficiency of the tandem device was calculated based on the operating current and the selectivity of generated products.

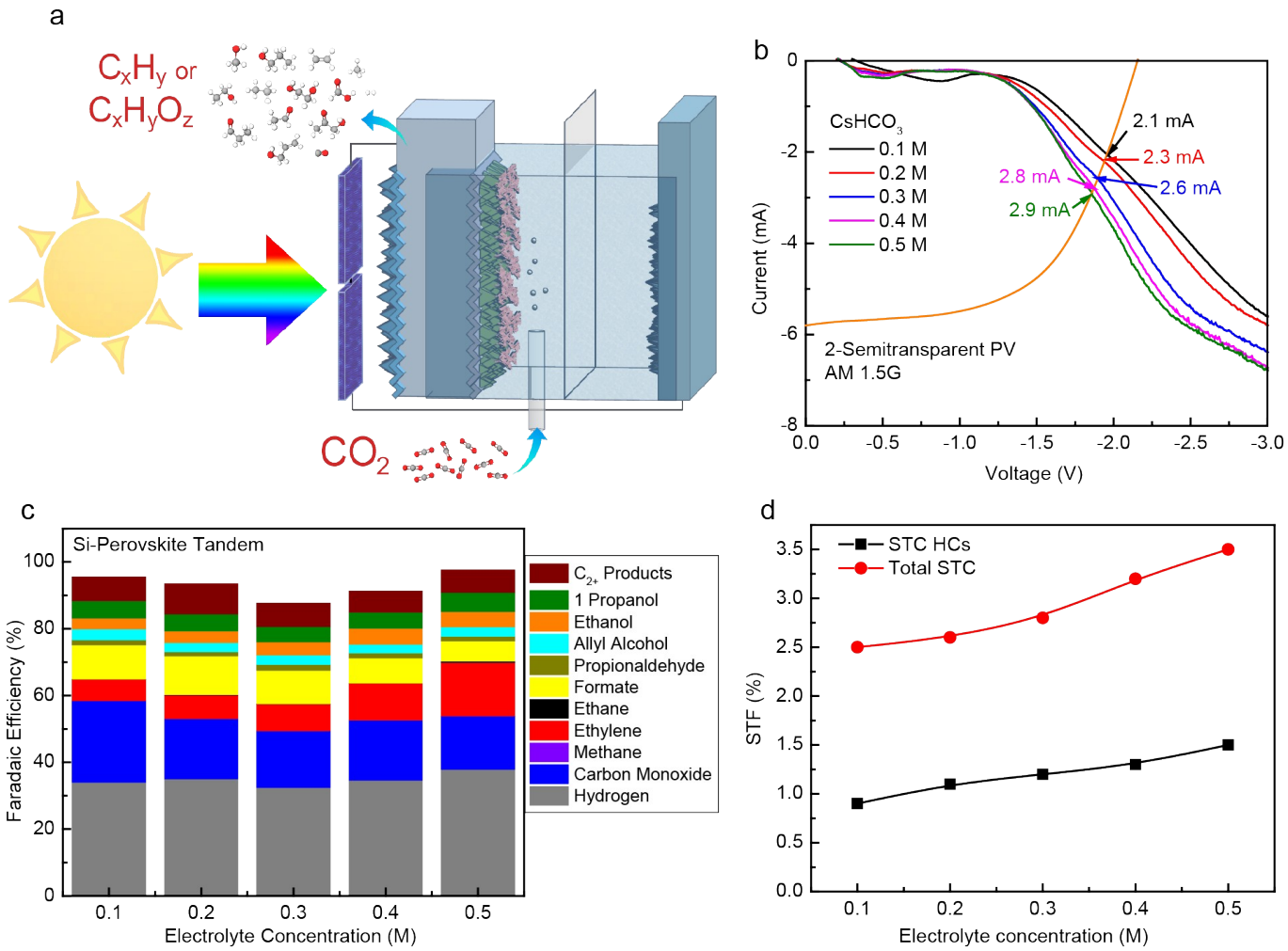

Figure 5. Solar-driven CO_2R measurements performed in a two-electrode configuration with a Si photocathode and an IrO_2 nanotube anode in tandem with two series-connected semi-transparent perovskite solar cells. **a,** Schematic of solar CO_2 reduction PV-PEC system. **b,** Measured current of top photoabsorbers (perovskite solar cells) and bottom photo absorber (Si photocathode) in various electrolyte conditions (0.1 – 0.5 M $CsHCO_3$) and under 1-sun illumination. Light reaching the Si photocathode is filtered via the top absorber;PEC measurements were performed in 2-electrode configuration. Intersection of these current shows the operating point of the device. **c,** CO_2 R product distribution of PV-PEC tandem device in 0.1 to 0.5 M $CsHCO_3$ and under 1-sun illumination. **d,** Solar-to-chemical conversion efficiency of PV-PEC device as a function of electrolyte concentration.

The solar to chemical conversion efficiency for all products increases with electrolyte concentration, going from 2.5% at 0.1 M to 3.5% at 0.5 M, Fig 5d. The efficiency for producing hydrocarbons and oxygenates also increases, going from 0.9% to 1.5% over the same range of electrolyte concentration. It could be expected that higher electrolyte concentration might yield even higher solar conversion efficiencies. However we found in our prior study which used a similar Ag-supported dendritic Cu CO_2R catalyst that electrolyte concentrations higher than 0.5 M decrease the C_{2+} product selectivity.[23]

Prospects for scale-up

The geometry we employed for the proof of principle self-powered CO_2R device, with the photovoltaic components beside the Si photocathode would require redesign to be scalable. However, we observe that there are precedents from stand-alone water splitting demonstrations showing that lateral interconnections and integration methods of the type we would need for scaling our design are technically feasible.[71,72] Also, Si-based water-splitting devices have been demonstrated at large scale (e.g. 64 cm^2 by Becker et al.[73]) and can be tiled into functional modules as shown by Turan et al.[74] The processes we used to prepare the photocathodes (texturing, ion implantation, ALD, metal evaporation) either were performed at the full wafer scale or could be done with existing commercial tools. The electrodeposition process used to deposit the Cu CO_2R catalyst also could be done on full Si wafers. Thus, we do not foresee any issues in producing Si photocathodes at the size of commercial PV cells, 6”×6”.

The cell design including the anion conducting membrane is conceptually similar to commercial fuel cells. IrO_2 and Pt, which we used as anode materials, are scarce and expensive and thus not favourable for large-scale application, so alternatives need to be found. In addition to the CoPi anode we investigated here,[75] manganese based ternary oxides and perovskites perform OER at neutral pH but require higher overpotentials than the Pt and IrO_2.[76,77] Thus, a less expensive

anode material with similar or better OER performance compared to IrO_2 would be desirable for scale-up.

Finally, regarding the perovskite solar cells, there are intense efforts ongoing world-wide to scale up this technology, which has inherent cost advantages compared to Si. In particular, there are a number of recent demonstrations of large area (10-100 cm^2) perovskite solar cells which could be used in tandem with Si-wafer-based CO_2R photocathodes in geometries similar to what we have demonstrated here.[78–80]

Conclusions

A back-illuminated n-type Si photoabsorber coupled with an Ag-supported dendritic Cu catalyst forms an effective photocathode for the photoelectrochemical CO_2 reduction in aqueous solution. Directional charge transport is enforced with charge-selective contacts while texturing of the Si increases light capture on the illumination side and increases the area available for electrocatalysts on the electrolyte side. Integration of an Ag supported dendritic Cu catalyst enables production of C_2 and C_3 products such as ethylene, ethanol, and 1-propanol. A catalyst regeneration method is demonstrated which mitigates contamination of the photocathode by metals from the anode, which occurs during multi-day operation. A strategy for coupling efficient PV to a Si photocathode is used for stand alone, "no bias," solar-driven CO_2 reduction, and a maximum total solar-to-chemical conversion efficiency of 3.5% to all products and 1.5% to hydrocarbons and oxygenates is reported. The modular nature of our approach allows for further improvements in solar-to-chemical conversion efficiency, which could be achieved by better power matching between the solar cells and the Si photocathode and improvements in the selectivity of the catalysts.

Conflicts of interest

There are no conflicts to declare.

Author contributions

JWA and G designed the study. G synthesized photocathode and anode materials and performed all photoelectrochemical (PEC) and PV/PEC analyses. G and JB designed the ion implantation protocol and JB performed the ion implantation. JA, G, NM, and WH selected the semi-transparent perovskites PV devices which were fabricated by WH. G performed PV and PV/PEC tandem efficiency measurements. G and CT analysed FE and PV efficiency data. JE and G performed and analysed the XPS data. AJ, JB, FMT, JE, and CMT contributed to discussions of the charge collection mechanism. The manuscript was written with contributions from all of the co-authors.

Acknowledgements

We acknowledge Prof. Subodh Mhaisalkar and Dr Herlina Arianita Dewi for discussions regarding the design of the semi-transparent perovskite solar cells. This material is based on the work supported by the Joint Centre for Artificial Photosynthesis (JCAP), a DOE Energy Innovation Hub, supported through the Office of Science of the U.S. Department of Energy under Award Number DE-SC0004993. Silicon texturing, photolithography and ion implantation were performed in the Electronic Materials Program, which is supported by the Director, Office of Science, Office of Basic Energy Sciences, Materials Sciences and Engineering Division, of the U.S. Department of Energy under Contract No. DE-AC02-05CH11231. Fabrication of perovskite solar cells was supported by the National Research Foundation, Prime Minister's Office, Singapore under its Competitive Research Programme (CRP Award No. NRF-CRP14-2014-03) and through the Singapore–Berkeley Research Initiative for Sustainable Energy (SinBeRISE) CREATE Program and by a Singapore Ministry of Education Tier 2 project (MOE2016-T2-2-012).

References

1 D. G. Nocera, *Chem. Soc. Rev.*, 2009, **38**, 13–15.
2 S. Chu and A. Majumdar, *Nature*, 2012, **488**, 294–303.
3 R. Shepherd, in *Climate Change 2013 - The Physical Science Basis*, ed. Intergovernmental Panel on Climate Change, Cambridge University Press, Cambridge, 2016, vol. 351, pp. 1–30.
4 C. Graves, S. D. Ebbesen, M. Mogensen and K. S. Lackner, *Renew. Sustain. Energy Rev.*, 2011, **15**, 1–23.
5 J. H. Golbeck, Ed., *Photosystem I: the light-driven plastocyanin: ferredoxin oxidoreductase*, Springer, 2006, vol. 24.
6 T. J. Wydrzynski and K. Satoh, Eds., *Photosystem II: the light-driven water: plastoquinone odixoreductase*, Springer, 2005, vol. 22.
7 D. G. Nocera, *Acc. Chem. Res.*, 2012, **45**, 767–76.
8 M. R. Singh and A. T. Bell, *Energy Environ. Sci.*, 2016, **9**, 193–199.
9 D. G. Nocera, *Acc. Chem. Res.*, 2017, **50**, 616–619.
10 F. E. Osterloh, *ACS Energy Lett.*, 2017, **2**, 445–453.
11 J. Rongé, T. Bosserez, D. Martel, C. Nervi, L. Boarino, F. Taulelle, G. Decher, S. Bordiga and J. A. Martens, *Chem. Soc. Rev.*, 2014, **43**, 7963–7981.
12 J. W. Ager, M. R. Shaner, K. A. Walczak, I. D. Sharp and S. Ardo, *Energy Environ. Sci.*, 2015, **8**, 2811–2824.
13 C. Xiang, A. Z. Weber, S. Ardo, A. Berger, Y. Chen, R. Coridan, K. T. Fountaine, S. Haussener, S. Hu, R. Liu, N. S. Lewis, M. A. Modestino, M. M. Shaner, M. R. Singh, J. C. Stevens, K. Sun and K. Walczak, *Angew. Chemie Int. Ed.*, 2016, **55**, 12974–12988.
14 J. Brillet, M. Cornuz, F. Le Formal, J.-H. Yum and M. Grätzel, *J. Mater. Res.*, 2010, **25**, 17.
15 A. C. Nielander, M. R. Shaner, K. M. Papadantonakis, S. A. Francis and N. S. Lewis, *Energy Environ. Sci.*, 2015, **8**, 16–25.

16 N. Gupta, M. Gattrell and B. MacDougall, *J. Appl. Electrochem.*, 2006, **36**, 161–172.

17 M. A. Green, K. Emery, Y. Hishikawa, W. Warta and E. D. Dunlop, *Prog. Photovoltaics Res. Appl.*, 2015, **23**, 805–812.

18 M. Schreier, L. Curvat, F. Giordano, L. Steier, A. Abate, S. M. Zakeeruddin, J. Luo, M. T. Mayer and M. Grätzel, *Nat. Commun.*, 2015, **6**, 7326.

19 H. S. Jeon, J. H. Koh, S. J. Park, M. S. Jee, D.-H. Ko, Y. J. Hwang and B. K. Min, *J. Mater. Chem. A*, 2015, **3**, 5835–5842.

20 T. Arai, S. Sato and T. Morikawa, *Energy Environ. Sci.*, 2015, **8**, 1998–2002.

21 X. Zhou, R. Liu, K. Sun, Y. Chen, E. Verlage, S. A. Francis, N. S. Lewis and C. Xiang, *ACS Energy Lett.*, 2016, **1**, 764–770.

22 M. Schreier, F. Héroguel, L. Steier, S. Ahmad, J. S. Luterbacher, M. T. Mayer, J. Luo and M. Grätzel, *Nat. Energy*, 2017, **2**, 17087.

23 Gurudayal, J. Bullock, D. F. Srankó, C. M. Towle, Y. Lum, M. Hettick, M. C. Scott, A. Javey and J. W. Ager, *Energy Environ. Sci.*, 2017, **10**, 2222–2230.

24 D. Ren, N. W. X. Loo, L. Gong and B. S. Yeo, *ACS Sustain. Chem. Eng.*, 2017, **5**, 9191–9199.

25 F. Urbain, P. Tang, N. M. Carretero, T. Andreu, L. G. Gerling, C. Voz, J. Arbiol and J. R. Morante, *Energy Environ. Sci.*, 2017, **10**, 2256–2266.

26 D. Marxer, P. Furler, M. Takacs and A. Steinfeld, *Energy Environ. Sci.*, 2017, **10**, 1142–1149.

27 M. Asadi, K. Kim, C. Liu, A. V. Addepalli, P. Abbasi, P. Yasaei, P. Phillips, A. Behranginia, J. M. Cerrato, R. Haasch, P. Zapol, B. Kumar, R. F. Klie, J. Abiade, L. A. Curtiss and A. Salehi-Khojin, *Science*, 2016, **353**, 467–470.

28 B. Kumar, M. Llorente, J. Froehlich, T. Dang, A. Sathrum and C. P. Kubiak, *Annu. Rev. Phys. Chem.*, 2012, **63**, 541–569.

29 S. N. Habisreutinger, L. Schmidt-Mende and J. K. Stolarczyk, *Angew. Chemie Int. Ed.*, 2013, **52**, 7372–7408.

30 J. L. White, M. F. Baruch, J. E. Pander III, Y. Hu, I. C. Fortmeyer, J. E. Park, T. Zhang, K. Liao, J. Gu, Y. Yan, T. W. Shaw, E. Abelev and A. B. Bocarsly, *Chem. Rev.*, 2015, **115**, 12888–12935.

31 C. Peng, G. Reid, H. Wang and P. Hu, *J. Chem. Phys.*, 2017, **147**, 030901.

32 M. Halmann, *Nature*, 1978, **275**, 115–116.

33 W. M. Sears and S. R. Morrison, *J. Phys. Chem.*, 1985, **89**, 3295–3298.

34 E. E. Barton, D. M. Rampulla and A. B. Bocarsly, *J. Am. Chem. Soc.*, 2008, **130**, 6342–6344.

35 B. Aurian-Blajeni, M. Halmann and J. Manassen, *Sol. Energy Mater.*, 1983, **8**, 425–440.

36 J. Qiu, G. Zeng, M.-A. Ha, M. Ge, Y. Lin, M. Hettick, B. Hou, A. N. Alexandrova, A. Javey and S. B. Cronin, *Nano Lett.*, 2015, **15**, 6177–6181.

37 C. Costentin, J. C. Canales, B. Haddou and J.-M. Savéant, *J. Am. Chem. Soc.*, 2013, **135**, 17671–17674.

38 J.-M. Saveant and C. Tard, *J. Am. Chem. Soc.*, 2016, **138**, 1017–1021.

39 H. Dridi, C. Comminges, C. Morais, J.-C. Meledje, K. B. Kokoh, C. Costentin and J.-M. Savéant, *J. Am. Chem. Soc.*, 2017, **139**, 13922–13928.

40 C. Costentin, J.-M. Savéant and C. Tard, *ACS Energy Lett.*, 2018, **3**, 695–703.

41 B. Kumar, J. M. Smieja and C. P. Kubiak, *J. Phys. Chem. C*, 2010, **114**, 14220–14223.

42 E. Torralba-Penalver, Y. Luo, J. D. Compain, S. Chardon-Noblat and B. Fabre, *ACS Catal.*, 2015, **5**, 6138–6147.

43 J. T. Song, H. Ryoo, M. Cho, J. Kim, J.-G. Kim, S.-Y. Chung and J. Oh, *Adv. Energy Mater.*, 2017, **7**, 1601103.

44 K. D. Yang, Y. Ha, U. Sim, J. An, C. W. Lee, K. Jin, Y. Kim, J. Park, J. S. Hong, J. H. Lee, H.-E. Lee, H.-Y. Jeong, H. Kim and K. T. Nam, *Adv. Funct. Mater.*, 2016, **26**, 233–242.

45 J. Shi, Y. Jiang, Z. Jiang, X. Wang, X. Wang, S. Zhang, P. Han and C. Yang, *Chem. Soc. Rev.*, 2015, **44**, 5981–6000.

46 O. S. Bushuyev, P. De Luna, C. T. Dinh, L. Tao, G. Saur, J. van de Lagemaat, S. O. Kelley and E. H. Sargent, *Joule*, 2018, **2**, 825–832.

47 Y. Hori, in *Modern Aspects of Electrochemistry*, Springer New York, New York, NY, 2008, vol. 29, pp. 89–189.

48 H. Mistry, A. S. Varela, S. Kühl, P. Strasser and B. R. Cuenya, *Nat. Rev. Mater.*, 2016, **1**, 16009.

49 M. Aresta, A. Dibenedetto and E. Quaranta, *J. Catal.*, 2016, **343**, 2–45.

50 B. Kumar, J. P. Brian, V. Atla, S. Kumari, K. A. Bertram, R. T. White and J. M. Spurgeon, *Catal. Today*, 2016, **270**, 19–30.

51 D. Ren, B. S.-H. Ang and B. S. Yeo, *ACS Catal.*, 2016, **6**, 8239–8247.

52 Q. Kong, D. Kim, C. Liu, Y. Yu, Y. Su, Y. Li and P. Yang, *Nano Lett.*, 2016, **16**, 5675–5680.

53 R. Hinogami, Y. Nakamura, S. Yae and Y. Nakato, *J. Phys. Chem. B*, 1998, **102**, 974–980.

54 P. Würfel and U. Würfel, *Physics of solar cells: from basic principles to advanced concepts*, Wiley, Weinheim, 2nd edn., 2009.

55 U. Wurfel, A. Cuevas and P. Wurfel, *IEEE J. Photovoltaics*, 2015, **5**, 461–469.

56 J. Bullock, M. Hettick, J. Geissbühler, A. J. Ong, T. Allen, C. M. Sutter-Fella, T. Chen, H. Ota, E. W. Schaler, S. De Wolf, C. Ballif, A. Cuevas and A. Javey, *Nat. Energy*, 2016, **1**, 15031.

57 F. Urbain, P. Tang, N. M. Carretero, T. Andreu, J. Arbiol and J. R. Morante, *ACS Appl. Mater. Interfaces*, 2018, **10**, 43650–43660.

58 D. Raciti, M. Mao, J. H. Park and C. Wang, *J. Electrochem. Soc.*, 2018, **165**, F799–F804.

59 Y. Lum, B. Yue, P. Lobaccaro, A. T. Bell and J. W. Ager, *J. Phys. Chem. C*, 2017, **121**, 14191–14203.

60 Y. S. Ham, S. Choe, M. J. Kim, T. Lim, S.-K. Kim and J. J. Kim, *Appl. Catal. B Environ.*, 2017, **208**, 35–43.

61 A. Murata and Y. Hori, *Bull. Chem. Soc. Jpn.*, 1991, **64**, 123–127.

62 M. R. Singh, Y. Kwon, Y. Lum, J. W. Ager and A. T. Bell, *J. Am. Chem. Soc.*, 2016, **138**, 13006–13012.

63 A. G. Scheuermann, J. P. Lawrence, K. W. Kemp, T. Ito, A. Walsh, C. E. D. Chidsey, P. K. Hurley and P. C. McIntyre, *Nat. Mater.*, 2015, **15**, 99–105.

64 L. Chen, J. Yang, S. Klaus, L. J. Lee, R. Woods-Robinson, J. Ma, Y. Lum, J. K. Cooper, F. M. Toma, L.-W. Wang, I. D.

Sharp, A. T. Bell and J. W. Ager, *J. Am. Chem. Soc.*, 2015, **137**, 9595–9603.
65 R. Hinogami, T. Mori, S. Yae and Y. Nakato, *Chem. Lett.*, 1994, 23, 1725–1728.
66 P. Zhai, S. Haussener, J. Ager, R. Sathre, K. Walczak, J. Greenblatt and T. McKone, *Energy Environ. Sci.*, 2013, **6**, 2380.
67 R. Sathre, C. D. Scown, W. R. Morrow, J. C. Stevens, I. D. Sharp, J. W. Ager, K. Walczak, F. A. Houle and J. B. Greenblatt, *Energy Environ. Sci.*, 2014, **7**, 3264–3278.
68 R. Sathre, J. B. Greenblatt, K. Walczak, I. D. Sharp, J. C. Stevens, J. W. Ager and F. A. Houle, *Energy Environ. Sci.*, 2016, **9**, 803–819.
69 Gurudayal, D. Sabba, M. H. Kumar, L. H. Wong, J. Barber, M. Grätzel and N. Mathews, *Nano Lett.*, 2015, **15**, 3833–3839.
70 Gurudayal, R. A. John, P. P. Boix, C. Yi, C. Shi, M. C. Scott, S. A. Veldhuis, A. M. Minor, S. M. Zakeeruddin, L. H. Wong, M. Grätzel and N. Mathews, *ChemSusChem*, 2017, **10**, 2449–2456.
71 T. J. Jacobsson, V. Fjallstrom, M. Sahlberg, M. Edoff and T. Edvinsson, *Energy Environ. Sci.*, 2013, **6**, 3676–3683.
72 D. Kang, J. L. Young, H. Lim, W. E. Klein, H. Chen, Y. Xi, B. Gai, T. G. Deutsch and J. Yoon, *Nat. Energy*, 2017, **2**, 17043.
73 J.-P. Becker, B. Turan, V. Smirnov, K. Welter, F. Urbain, J. Wolff, S. Haas and F. Finger, *J. Mater. Chem. A*, 2017, **5**, 4818–4826.
74 B. Turan, J.-P. Becker, F. Urbain, F. Finger, U. Rau and S. Haas, *Nat. Commun.*, 2016, **7**, 12681.
75 M. W. Kanan and D. G. Nocera, *Science*, 2008, **321**, 1072–1075.
76 D. Jeong, K. Jin, S. E. Jerng, H. Seo, D. Kim, S. H. Nahm, S. H. Kim and K. T. Nam, *ACS Catal.*, 2015, **5**, 4624–4628.
77 B. Han, M. Risch, Y.-L. Lee, C. Ling, H. Jia and Y. Shao-Horn, *Phys. Chem. Chem. Phys.*, 2015, **17**, 22576–22580.
78 A. Bashir, S. Shukla, J. H. Lew, S. Shukla, A. Bruno, D. Gupta, T. Baikie, R. Patidar, Z. Akhter, A. Priyadarshi, N. Mathews and S. G. Mhaisalkar, *Nanoscale*, 2018, **10**, 2341–2350.
79 H. Chen, F. Ye, W. Tang, J. He, M. Yin, Y. Wang, F. Xie, E. Bi, X. Yang, M. Grätzel and L. Han, *Nature*, 2017, **550**, 92–95.
80 S. Razza, F. Di Giacomo, F. Matteocci, L. Cinà, A. L. Palma, S. Casaluci, P. Cameron, A. D'Epifanio, S. Licoccia, A. Reale, T. M. Brown and A. Di Carlo, *J. Power Sources*, 2015, **277**, 286–291.